

Double refraction and spin splitter in a normal-hexagonal semiconductor junction

Peng Lv,¹ Ning Dai,¹ and Qing-Feng Sun^{1,2,*}

¹International Center for Quantum Materials, School of Physics, Peking University, Beijing 100871, China

²Collaborative Innovation Center of Quantum Matter, Beijing, 100871, China

In analogy with light refraction at optical boundary, ballistic electrons also undergo refraction when propagate across a semiconductor junction. Establishing a negative refractive index in conventional optical materials is difficult, but the realization of negative refraction in electronic system is conceptually straightforward, which has been verified in graphene p-n junctions in recent experiments. Here, we propose a model to realize double refraction and double focusing of electric current by a normal-hexagonal semiconductor junction. The double refraction can be either positive or negative, depending on the junction being n-n type or p-n type. Based on the valley-dependent negative refraction, a spin splitter (valley splitter) is designed at the p-n junction system, where the spin-up and spin-down electrons are focused at different regions. These findings may be useful for the engineering of double lenses in electronic system and have underlying application of spin splitter in spintronics.

PACS numbers:

I. INTRODUCTION

The propagation of electrons has many similarities with the propagation of light.^{1,2} In two-dimensional electron gas (2DEG), where the mean free path is larger than the size of the system, ballistic electrons propagate following straight-line trajectories which is analogous to light rays. When the ballistic electrons transmit across a semiconductor junction, electrons should undergo refraction in analogy with light refraction at optical boundary with different refractive indices.³⁻⁶ Such phenomena can be understood simply in terms of Snell's law, where the refractive index of photons is replaced by the wave vector of electrons. Thus, it is possible to manipulate electrons like photons and electron optics has attracted worldwide attention because of its underlying applications. Electron focusing, diffraction, and double-slit interference experiments are examples of electron optics which have been clearly observed in 2DEG systems.^{7,8}

In conventional 2DEG systems, electrostatic lenses have been demonstrated in high mobility GaAs about thirty years ago.^{3,4} Since then, many work have been undertaken to obtain various electron optical devices like mirrors, prisms, lenses and splitters.⁹⁻¹³ One interesting topic of electron optics is the negative refraction,^{14,15} which is challenging to achieve in conventional optical systems. For photons, this behavior can be realized in optical metamaterials.^{16,17} In electronic systems, negative refraction can be achieved quite straightforward.^{9,18} For example, when electrons transmit across a p-n junction, in order to conserve the transverse component of momentum, the transverse group velocity has to change a sign between the valence bands in p side and the conduction bands in n side, hence leads to the negative refraction. Graphene has a unique band structure with a linear dispersion relation of low-lying excitations, which gives rise to many peculiar properties.^{19,20} Because of the vanishing band gap and the high intrinsic mobility, graphene has also been considered as an attractive

platform for studying the electron optics.^{9-12,21-24} Recent experiments have clearly demonstrated the negative refraction in graphene p-n junctions.^{18,23} This negative refraction can be used to design a perfect lens, and has many other potential applications.

In optics, a beam of light at the anisotropic crystal interface exhibits the double refraction effects. Recently, monolayer transition-metal dichalcogenides (TMDs) have been successfully fabricated in experiments.²⁵⁻²⁹ The TMDs (e.g. NbSe₂, MoS₂) exhibit Ising pairing in superconducting phase at sufficiently low temperature, with an in-plane upper critical field far above the Pauli paramagnetic limit.²⁵⁻²⁸ This unusual behavior is attributed to the inter-valley pairing protected by Zeeman-type spin-valley locking against external magnetic fields.²⁶ This out-of-plane Zeeman-type spin polarization of the valleys can be used to achieve double refraction in electron optics. Motivated by this, in this paper, we propose a model to realize double refraction and double focusing of electric current by a normal-hexagonal semiconductor junction. This model is based on a hexagonal lattice system (like graphene or TMDs), but breaks the A-B lattice symmetry. By introducing a Rashba spin-orbit interaction into the system, the two valleys in the Brillouin zone are no longer equivalent. When an electron is incident from the normal conductor side with the square lattice, double refraction and double focusing occur, and the electron is transmitted to two different modes. The two modes have different refractive indices due to the two valleys being inequivalent. We investigate electron optics in both n-n junction and p-n junction below. In particular, the incident electron undergoes double negative refraction in p-n junction. We also show that by double negative refraction with elaborately tuning the chemical potential of the system, the p-n junction can work as a spin splitter (valley splitter), which may be useful in spintronics (valleytronics).

The rest of this paper is organized as follows. In Sec. II, we present the model Hamiltonian and the corre-

sponding band structures of the normal-hexagonal semiconductor junction, considering both the effect of A-B lattice symmetry breaking and Rashba spin-orbit interaction. In Sec. III, we investigate the positive double refraction in n-n junction and the negative double refraction in p-n junction. In Sec. IV, a spin splitter is designed based on the negative double refraction. Finally, a brief summary is presented in Sec V.

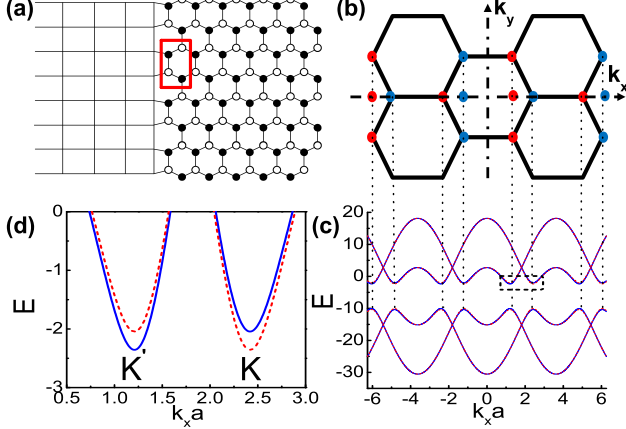


FIG. 1: (Color online) Lattice diagram and band structures. (a) The schematic diagram of the normal-hexagonal semiconductor junction in the lattice model. (b) Brillouin zone of the hexagonal lattice. (c) Energy bands along the dash line in (b) in which $k_y = 0$. Dashed red lines denote the energy bands of spin-up electrons, while the blue lines are the spin-down bands. (d) Zoom-in figure of the energy bands of the dotted box in (c). The parameters are $\epsilon_R = -6.2$, $t_R = -8$, $\beta = 4$, and $\beta_s = -0.03$.

II. MODEL HAMILTONIAN AND BAND STRUCTURES

In the following, we introduce the model Hamiltonian and demonstrate the corresponding band structures. Fig. 1a is the lattice model of the normal-hexagonal semiconductor junction, which consists of a square lattice at the left side and a hexagonal lattice at the right side. The Hamiltonian of the whole system can be written as

$$H = H_L + H_R + H_T, \quad (1)$$

where H_L , H_R , H_T are the Hamiltonians of the normal, hexagonal semiconductors, and the coupling between them, respectively. For the normal conductor, we consider the square lattice model with the dispersion relation of its carrier being quadratic. In the tight-binding representation, the Hamiltonian H_L is of the form^{30,31}

$$H_L = \sum_{i\sigma} \epsilon_L a_{i\sigma}^\dagger a_{i\sigma} + \sum_{\langle ij \rangle \sigma} t_L a_{i\sigma}^\dagger a_{j\sigma}, \quad (2)$$

where $a_{i\sigma}$ and $a_{i\sigma}^\dagger$ are the annihilation and creation operators at the discrete site i , and ϵ_L is the on-site energy.

The second term in equation (2) is the nearest-neighbor hopping. t_L is the hopping energy, which is positive for valence bands and negative for conduction bands. Experimentally, it is possible to break the A-B lattice symmetry in a hexagonal lattice like graphene. For example, isolated graphene/BN bilayers break the chemical equivalence of graphene A and B lattice sites.^{32,33} Graphene growth on the reconstructed surface of MgO(111) also leads to A-B lattice symmetry breaking.^{34,35} In addition, spin-orbit interaction can also play a very important role in some two-dimensional materials. The emergence of the quantum spin Hall effect and topological insulators can be attributed to the rise of the spin-orbit interaction.³⁶⁻³⁹ Thus, we consider a general Hamiltonian at the hexagonal lattice side as

$$H_R = \sum_{i\sigma} (\epsilon_R + \lambda_i \beta) b_{i\sigma}^\dagger b_{i\sigma} + \sum_{\langle ij \rangle \sigma} t_R b_{i\sigma}^\dagger b_{j\sigma} + \sum_{\langle\langle ij \rangle\rangle \sigma \sigma'} i \beta_s \nu_{ij} s_{\sigma\sigma'}^z b_{i\sigma}^\dagger b_{j\sigma'}, \quad (3)$$

where $b_{i\sigma}$ and $b_{i\sigma}^\dagger$ are the annihilation and creation operators at the discrete site i of the right side. ϵ_R is the on-site energy, and β represents the energy difference between A-B sublattice. Here $\lambda_i = \pm 1$ for A(B)-sublattice. The second term is the nearest-neighbor hopping term, and t_R is the hopping energy. The third term is the spin-orbit interaction which connects second nearest neighbor. The same term also appears in the seminal work of the quantum spin Hall effect in graphene.³⁶ s_z is a Pauli matrix representing the electron's spin and $\nu_{ij} = -\nu_{ji} = \pm 1$ depending on the orientation of the two site i to j .³⁶ The spin-orbit coupling β_s is usually very small comparing to t_R , but it can be in the order of meV by the Bi-cluster deposition.⁴⁰ The Hamiltonian H_T of the coupling between the left and right lead is

$$H_T = \sum_{ij\sigma} t_c a_{i\sigma}^\dagger b_{j\sigma} + h.c. \quad (4)$$

where t_c is the coupling strength. Here we assume that the interface of the normal and hexagonal semiconductors are perfect (see Fig.1a). In usual, there are defects in the real devices and the interface is rough as well. While the incident and refractive electrons are in the bottom of the conduction band or the top of the valence band, their wavelengths are usually very long. As long as the wavelength is much longer than the defect size and the interface roughness, the direction of the refraction can be well maintained and the results are barely affected by the defect and the imperfect interface.

The Brillouin zone of the hexagonal lattice is demonstrated in Fig.1b. We choose each unit cell containing four atoms (see red box in Fig.1a) which can simplify the calculations of the transmission coefficients, hence the Brillouin zone is one half smaller than the usual Brillouin zone of graphene. In Fig.1c, we plot the energy bands along the dashed line in Fig.1b with $k_y = 0$. Because of the Brillouin zone being half smaller, the number

of the energy bands is double, and each spin orientation has four energy bands. Breaking the A-B lattice symmetry induces a big energy gap at the K and K' points. We mainly consider the electrons transport near the Fermi surface, and the four lower energy bands can be ignored, as they are much below the Fermi surface $E = 0$. In Fig.1d, the zoom-in figure of the energy bands near the K and K' points are presented. The spin-orbit coupling can be viewed as an effective magnetic field \mathbf{B} that points in the opposite directions at the K and K' points. At K point, spin up electrons have lower energy while at K' point the other way around. Thus, for energy bands with a definite spin orientation, the energy dispersion relation between the K and K' points are no longer equivalent any more. In fact, this energy band is the same as that of TMDs in the normal phase.²⁹ So a junction consisting of a normal conductor coupled with the TMDs can be regarded as a real example of our model. Double refraction occurs when electrons incident from normal conductor with the square lattice side transmit to the two valleys, as demonstrated in the next section.

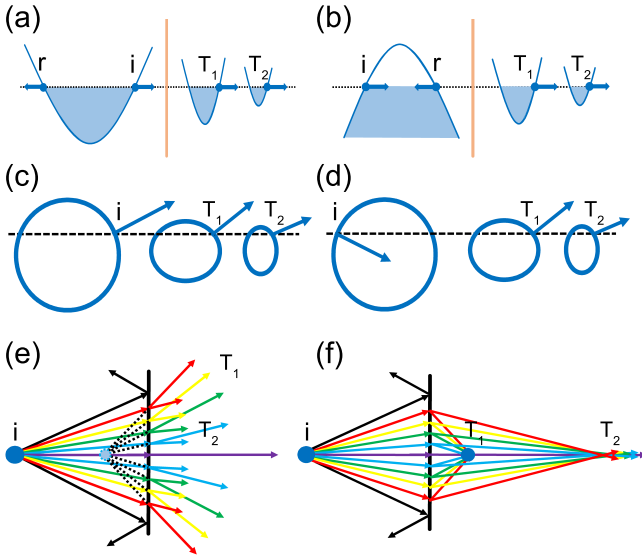


FIG. 2: (Color online) Heterojunction band diagrams and schematic of double refraction. (a) The band diagrams of the n-n junction. Incident electron i transmits to the two valleys with the transmission coefficients T_1 and T_2 . (b) The corresponding p-n junction case. (c) and (d) are the corresponding equienergy lines in the k_x - k_y plane for the n-n junction in (a) and the p-n junction in (b). Here the arrows indicate the directions of the incident and refraction carriers. (e) Schematic of the double positive refraction in the n-n junction. Electrons emitted from the source i are bent different amounts at the n-n junction interface, forming two virtual foci at the same side of the electron source. Only one virtual focus is plotted in (e). (f) Schematic of the double negative refraction in the p-n junction. Electrons emitted from the source i undergo double negative refraction at the p-n junction interface, forming two real focus at the opposite side of the electron source.

III. DOUBLE REFRACTION AND DOUBLE FOCUSING

In this section, we demonstrate how the normal-hexagonal semiconductor junctions leads to the double refraction and double focusing. Due to the Pauli matrix σ_z commuting with the Hamiltonian in Eq.(1), the spin in the z direction is conserved in the scattering process. So in the following analysis, we first consider a spin component, e.g. spin-up one. Fig.2a and 2b respectively illustrate the band diagrams of the n-n junction and p-n junction for a spin component, and the corresponding equienergy lines in the k_x - k_y plane are shown in Fig.2c and 2d. For an incident carrier (electron or hole) from the left normal conductor, there are two beams of outgoing electrons, due to the two non-equivalent valleys. Notice that the directions of the two beams of outgoing electrons are usually different. So the double refraction occurs in this normal-hexagonal semiconductor junction. Because of the transverse translation invariance in the model, the transverse component of the momentum (k_y) is conserved when electrons transmit across the junction. So the transverse group velocity preserves the sign between the n-n junction (see Fig.2c), but changes a sign between the valence bands in the p side and the conduction bands in the n side (see Fig.2d). As a consequence, the double refraction is positive in a n-n junction, while negative in a p-n junction. Fig.2e and 2f are the schematic diagrams of the positive and negative double reflections, respectively. For the positive double refraction, the outgoing electrons are bent different amounts as they pass through the junction and form two virtual foci at the same side of the electron source i . However, in Fig.2f, two real focuses are formed at the opposite side of the electron source, attributing to the opposite transverse velocity and the negative refractive index.

To further investigate the nature of the double refraction, we calculate the transmission coefficients and the refractive indices for both case in detail. By applying the non-equilibrium Green's function method to the tight-binding Hamiltonian H in equation (1), the transmission coefficients T_1 and T_2 can be obtained quite straightforward by following the same procedure as in Refs.[41,42]. Fig.3 displays the case of the double positive refraction in a n-n junction, where (a) and (b) are the transmission coefficients and (c) and (d) are the refractive indices. For small incident angle, the transmission coefficient T_1 is nearly a constant, and is insensitive to the incident energy E . As the incident angle increases, T_1 rapidly reduces and T_2 significantly increases. For large incident angle, both T_1 and T_2 drop to zero, attributing to the absence of the corresponding transmission modes at the n side. Thus, electrons undergo total reflection at large incident angle. Note that T_1 dominates the whole scattering process for a large range of parameters. The increasing of the incident energy enhance T_1 at large incident angle, but meanwhile suppress the transmission coefficient T_2 . The total transmission probability $T = T_1 + T_2 \approx 1$

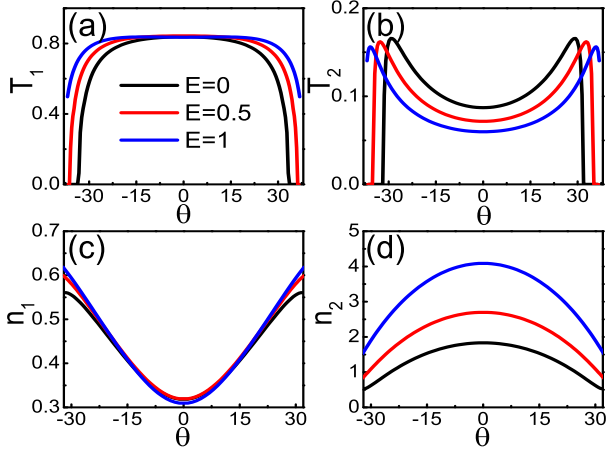


FIG. 3: (Color online) Transmission coefficients and refractive indices for the n-n junction. (a) and (b) are the transmission coefficients T_1 and T_2 at the two valleys as a function of the incident angle θ for the different incident energy E . (c) and (d) are the corresponding refractive indices. The parameters are $\epsilon_L = 7$, $t_L = -8$, others are the same as that in Fig.1 .

indicates that the n-n junction is almost transparent for the electrons. Meanwhile, the two transmission modes have different refractive property as shown in Fig.3c and 3d. Here the refractive index is define as $n_i = \sin \theta / \sin \theta_i$, where θ is the incident angle and θ_i ($i = 1, 2$) is the refraction angle of transmission mode i . The refractive index n_1 is insensitive to the incident energy, and increases as the incident angle grows. We emphasize that $n < 1$ for a large range of parameters, hence the electronic refraction at this valley serves as optically thinner medium in optics. For a perfect virtual focus, the refractive index n obeys the law $n^2 = c + (1 - c) \sin^2 \theta$, where the parameter $0 < c < 1$ in optically thinner medium. The refractive index n_1 approximately follows this law, hence this virtual focus is nearly perfect (see Fig.2e). For the refraction at the other valley, the refractive index $n > 1$ for a large range of parameters, hence electronic refraction at this valley serves as optically denser medium in optics. Here $c > 1$ in the optically denser medium. Although n_2 is sensitive to incident energy, it also approximate matches the law $n^2 = c + (1 - c) \sin^2 \theta$. Therefore, the second virtual focus is also relatively good (The second virtual focus is plotted in Fig.2e).

Next, we focus on the p-n junction in which the double negative refraction occurs, as illustrated in Fig.4. The main features of the transmission coefficients are basically the same as the case of positive refraction, except the position of T_1 and T_2 are changed. In this case, T_2 dominates the scattering process (see Fig.4a and 4b), but T_1 is not very small and it has the same order of T_2 . As for the refractive indices shown in Fig.4c and 4d, n_1 and n_2 become negative and almost have a mirror symmetry with the positive refractive indices in Fig.3c and 3d about the axis $n = 0$. Contrary to the previous case,

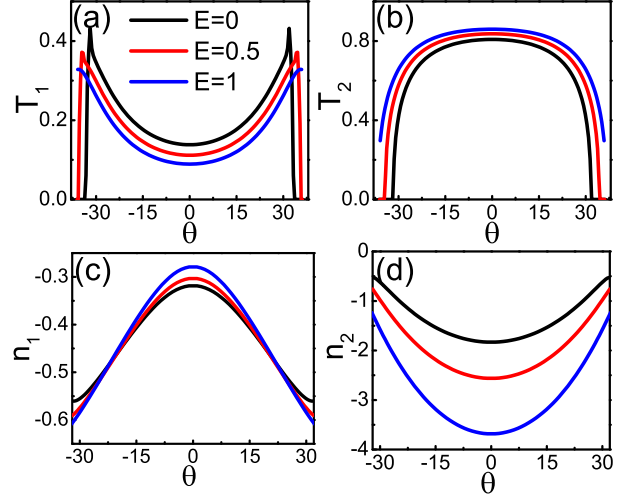


FIG. 4: (Color online) Transmission coefficients and refractive indices for the p-n junction. (a) and (b) are the transmission coefficients T_1 and T_2 at the two valleys versus the incident angle θ for the different incident energy E . (c) and (d) are the corresponding refractive indices. The parameters are $\epsilon_L = -7$, $t_L = 8$, others are the same as that in Fig.1 .

two real focus are formed at the opposite side of the electron source, and the focusing performance of the incident electrons is pretty good (see Fig. 2f).

The spin-down electrons show similar refractive behaviors at the two valleys. The double refraction is positive for a n-n junction and negative for a p-n junction, and the absolute value of the refractive index $|n| > 1$ at one valley and $|n| < 1$ at the other. Because of the time reversal invariance of our Hamiltonian, the scattering matrix of the spin-up and spin-down electrons satisfy the relation $\mathbf{s}_\uparrow^T = \mathbf{s}_\downarrow$, which indicates that $T_{1\uparrow} + T_{2\uparrow} = T_{1\downarrow} + T_{2\downarrow}$.

IV. SPIN SPLITTER AND DETECTIVE DEVICE

Spin-orbit coupling modifies the electronic band structures at the two valleys and the double refraction become spin dependent as mentioned above. Thus, for spin non-polarized incident electrons from the left side, the outgoing electrons on the right side will be spin-polarized, i.e. the normal-hexagonal semiconductor junction can be worked as a spin splitter. Below, as an example, we consider the p-n junction system, and the energy bands are shown in Fig.5a. Here the red lines denote the energy bands of spin-up electrons on the n side while the blue lines denote spin-down ones, and the green lines are the bands on the p side where the spin-up and spin-down electrons are degenerate. In order to clearly illustrate the physical picture of the spin splitter, the Fermi energy E is set to locate between the red line and blue line (see Fig.5a). In this case, the incident spin-up electrons can

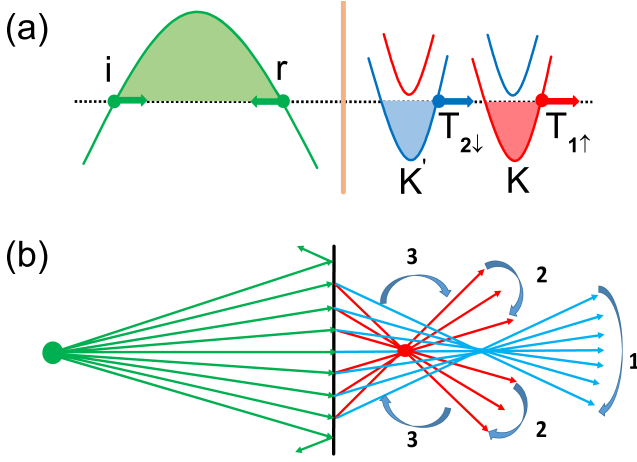


FIG. 5: (Color online) A spin splitter based on the normal-hexagonal p-n junction. (a) is the band diagrams of the spin splitter based on the normal-hexagonal p-n junction. Here the Fermi energy E locates between the energy bands of the up-spin and down-spin species of the n side. (b) is the schematic diagram of the electron's trajectory in the spin splitter. Electrons with different spin are separated in real space and focus in different regions.

only get through the junction via valley K at the state $T_{1\uparrow}$ while the spin-down electrons via valley K' at the state $T_{2\downarrow}$. Notice the states $T_{1\uparrow}$ and $T_{2\downarrow}$ are not mutually the time-reversal states and the dispersion relations at the two valleys $\epsilon_{K\uparrow}(\mathbf{k} - \mathbf{K}) \neq \epsilon_{K'\downarrow}(\mathbf{k} - \mathbf{K}')$, although the system has the time-reversal invariance with the dispersion relations having $\epsilon_{K\uparrow}(\mathbf{k} - \mathbf{K}) = \epsilon_{K'\downarrow}(-\mathbf{k} - \mathbf{K}')$. So the refractive indices of the two valleys are different, leading that the electrons with different spin are separated in real space and focus in different regions. By detailed calculation of the incident and refraction angles, we plot the schematic diagram of the electron's trajectory in Fig.5b. Spin-up electrons focus in a small area while spin-down electrons focus in a relatively large area. The electron's outgoing area can be divided in three regions. In region 1, both spin-up and spin-down electrons can be observed, but spin-down electrons are in the majority. In region 2, only spin-up outgoing electrons could be observed. In region 3, we can hardly detect any outgoing electron. In particular, at two focal points the density of the spin-up and spin-down outgoing electrons are very high, which can be detected by using ferromagnetic STM. Note that here the spin-up and spin-down electrons are at the valleys K and K', respectively. So the spin splitter is also a valley splitter.

Let us study the transmission coefficients and refractive indices of the spin splitter. Fig.6a and 6b are the transmission coefficients $T_{1\uparrow}$ and $T_{2\downarrow}$ of the two transport channels. The two transmission coefficients are in fact identical for various incident energy. This is because for each spin there is only one transmission mode, and the general relation $T_{1\uparrow} + T_{2\uparrow} = T_{1\downarrow} + T_{2\downarrow}$ reduces to

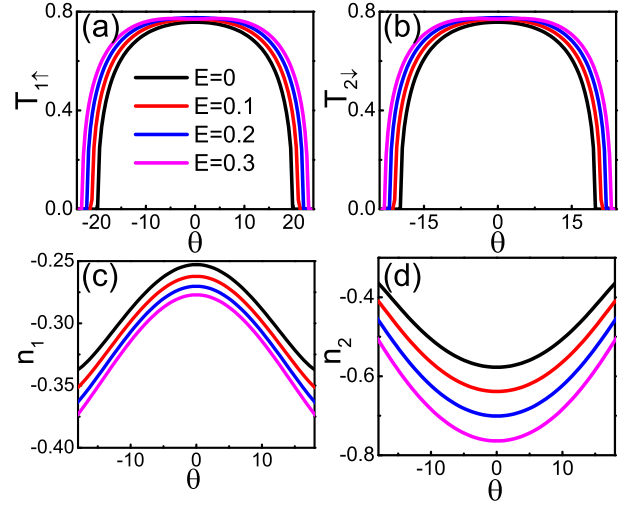


FIG. 6: (Color online) Transmission coefficients and refractive indices for the spin splitter. (a) and (b) are the transmission coefficients $T_{1\uparrow}$ and $T_{2\downarrow}$ for spin-up and spin-down electrons, respectively. (c) and (d) are the corresponding refractive indices. The parameters are $\epsilon_R = -4.2$, $t_R = 8$, $\beta = 4$, $\beta_s = -0.1$, $\epsilon_L = -7$ and $t_L = 8$.

$T_{1\uparrow} = T_{2\downarrow}$ in present case. $T_{1\uparrow}$ and $T_{2\downarrow}$ are the maximum when the incident angle $\theta = 0$. With the increase of θ , they decrease. And at large θ , $T_{1\uparrow}$ and $T_{2\downarrow}$ drops rapidly to zero. However, due to the band structures at the two valleys being not completely the same, the refractive indices present different behavior as illustrated in Fig.6c and 6d. With larger incident angle, the refractive index n_1 decreases, while n_2 shows opposite behavior. The refractive index n_1 approximately follows the asymptotic behaviour of perfect lenses, and the spin-up electrons focus in a small area. However, n_2 obviously do not follow the law, and the spin-down electrons focus in a relatively large area. Note that by changing the spin-orbit coupling constant β_s , different types of focusing pattern can be realised.

V. SUMMARY

In conclusion, we have proposed a model to realize double refraction and double focusing of electric current using a normal-hexagonal semiconductor junction. By breaking the A-B lattice symmetry and introducing the Rashba spin-orbit interaction, a large energy gap is formed and spin-up and spin-down electrons experience opposite effective magnetic field at the two valleys. Incident electrons transmit to the two valleys, and result in a double refraction at the hexagonal lattice side. The double refraction can be either positive or negative, depending on the junction being n-n type or p-n type. The two valleys reveal different type of refractive behaviors. The absolute value of the refractive index $|n| > 1$ at one

valley and $|n| < 1$ at the other. Additionally, the p-n junction can be used as a spin splitter (valley splitter), which could be verified by the ferromagnetic STM. Our results may be useful for the engineering of double lenses in electronic system and have underlying application in spintronics.

Acknowledgement

This work was financially supported by National Key R and D Program of China (2017YFA0303301), NBRP

of China (2015CB921102) and NSF-China under Grants Nos. 11574007 and 11274364.

References

-
- * sunqf@pku.edu.cn
- ¹ S. Datta, *Electronic transport in mesoscopic systems* (Cambridge University Press, England, 1995).
 - ² W. van Haeringen and D. Lenstra, *Analogies in optics and microelectronics* (Kluwer Academic Publishers, Netherlands, 1990).
 - ³ U. Sivan, M. Heiblum, C. P. Umbach, and H. Shtrikman, Phys. Rev. B **41**, 7937 (1990).
 - ⁴ J. Spector, H. L. Stormer, K. W. Baldwin, L. N. Pfeiffer, and K. W. West, Appl. Phys. Lett. **56**, 1290 (1990).
 - ⁵ C. W. J. Beenakker and H. van Houten, Solid State Phys. **44**, 1 (1991).
 - ⁶ P. Lv, A. M. Guo, H. Y. Li, C. X. Liu, X. C. Xie, and Q.-F. Sun, Phys. Rev. B **95**, 104516 (2017).
 - ⁷ H. van Houten, C. W. J. Beenakker, J. G. Williamson, M. E. I. Broekaart, P. H. M. van Loosdrecht, B. J. van Wees, J. E. Mooij, C. T. Foxon, and J. J. Harris, Phys. Rev. B **39**, 8556 (1989).
 - ⁸ A. Yacoby, U. Sivan, C. P. Umbach, and J. M. Hong, Phys. Rev. Lett. **66**, 1938 (1991).
 - ⁹ V. V. Cheianov, V. Fal'ko, and B. L. Altshuler, Science **315**, 1252 (2007).
 - ¹⁰ C.-H. Park, Y.-W. Son, L. Yang, M. L. Cohen, and S. G. Louie, Nano Lett. **8**, 2920 (2008).
 - ¹¹ M. S. Jang, H. Kim, Y.-W. Son, H. A. Atwater, and W. A. Goddard, Proc. Natl. Acad. Sci. **110**, 8786 (2013).
 - ¹² P. Rickhaus, P. Makk, M.-H. Liu, K. Richter, and C. Schönenberger, Appl. Phys. Lett. **107**, 251901 (2015).
 - ¹³ R. D. Y. Hills, A. Kusmartseva, and F. V. Kusmartsev, Phys. Rev. B **95**, 214103 (2017).
 - ¹⁴ V. G. Veselago, Sov. Phys. Usp. **10**, 509 (1968).
 - ¹⁵ J. B. Pendry, Phys. Rev. Lett. **85**, 3966 (2000).
 - ¹⁶ V. M. Shalaev, Nat. Photonics **1**, 41 (2007).
 - ¹⁷ R. A. Shelby, D. R. Smith, and S. Schultz, Science **292**, 77 (2001).
 - ¹⁸ S. W. Chen, *et al.* Science **353**, 1522 (2016).
 - ¹⁹ A. H. Castro Neto, F. Guinea, N. M. R. Peres, and K. S. Novoselov, Rev. Mod. Phys. **81**, 109 (2009).
 - ²⁰ L.-J. Yin, K.-K. Bai, W.-X. Wang, S.-Y. Li, Y. Zhang, and L. He, Front. Phys. **12**, 127208 (2017).
 - ²¹ P. Rickhaus, R. Maurand, M. H. Liu, M. Weiss, K. Richter, and C. Schönenberger, Nat. Commun. **4**, 2342 (2013).
 - ²² A. F. Young and P. Kim, Nat. Phys. **5**, 222 (2009).
 - ²³ G.-H. Lee, G.-H. Park, and H.-J. Lee, Nat. Phys. **11**, 925 (2015).
 - ²⁴ J.-C. Chen, X. C. Xie, and Q.-F. Sun, Phys. Rev. B **86**, 035429 (2012).
 - ²⁵ X. X. Xi, Z. F. Wang, W. W. Zhao, J.-H. Park, K. T. Law, H. Berger, L. Forró, J. Shan, and K. F. Mak, Nat. Phys. **12**, 139 (2016).
 - ²⁶ Y. Saito, *et al.* Nat. Phys. **12**, 144 (2016).
 - ²⁷ J. M. Lu, O. Zheliuk, I. Leermakers, N. F. Q. Yuan, U. Zeitler, K. T. Law, and J. T. Ye, Science **350**, 1353 (2015).
 - ²⁸ L. Bawden, *et al.* Nat. Commun. **7**, 11711 (2016).
 - ²⁹ B. T. Zhou, F. Q. Yuan, H.-L. Jiang, and K. T. Law, Phys. Rev. B **93**, 180501 (2016).
 - ³⁰ S.-G. Cheng, Y. X. Xing, Q.-F. Sun, and X. C. Xie, Phys. Rev. B **78**, 045302 (2008).
 - ³¹ Q.-F. Sun and X. C. Xie, J. Phys.: Condens. Matter **21**, 344204 (2009).
 - ³² G. Giovannetti, P. A. Khomyakov, G. Brocks, P. J. Kelly, and J. van den Brink, Phys. Rev. B **76**, 073103 (2007).
 - ³³ L. Kong, C. Bjelkevig, S. Gaddam, M. Zhou, Y. H. Lee, G. H. Han, H. K. Jeong, N. Wu, Z. Zhang, J. Xiao, P. A. Dowben, and J. A. Kelber, J. Phys. Chem. C **114**, 21618 (2010).
 - ³⁴ S. Gaddam, C. Bjelkevig, S. Ge, K. Fukutani, P. A. Dowben, and J. A. Kelber, J. Phys.: Condens. Matter **23**, 072204 (2011).
 - ³⁵ R. Skomski, P. A. Dowben, M. S. Driver, and J. A. Kelber, Mater. Horiz. **1**, 563 (2014).
 - ³⁶ C. L. Kane and E. J. Mele, Phys. Rev. Lett. **95**, 226801 (2005).
 - ³⁷ Q.-F. Sun and X. C. Xie, Phys. Rev. Lett. **104**, 066805 (2010).
 - ³⁸ M. Z. Hasan and C. L. Kane, Rev. Mod. Phys. **82**, 3045 (2010).
 - ³⁹ X.-L. Qi and S.-C. Zhang, Rev. Mod. Phys. **83**, 1057 (2011).
 - ⁴⁰ J.-L. Ge, T.-R. Wu, M. Gao, Z.-B. Bai, L. Cao, X.-F. Wang, Y.-Y. Qin, and F.-Q. Song, Front. Phys. **12**, 127210 (2017).
 - ⁴¹ N. Dai and Q.-F. Sun, Phys. Rev. B **95**, 064205 (2017).
 - ⁴² S. Sanvito, C. J. Lambert, J. H. Jefferson, and A. M. Bratkovsky, Phys. Rev. B **59**, 11936 (1999).